Complex-Based Controller for a Three-Phase Inverter With an *LCL* Filter Connected to Unbalanced Grids

Arnau Dòria-Cerezo, Federico Martín Serra, *Member, IEEE*, and Marc Bodson, *Fellow, IEEE*

***Abstract*—A new controller for a grid-connected inverter with an *LCL* filter is proposed in this paper. The system is described by its complex representation, and the controller is designed using the complex root locus method. The complex representation allows a considerable reduction in the order of the system, simplifying the design task and making it possible to use advanced techniques, such as the complex root locus. The new complex controller adds an extra degree of freedom that makes it possible to move the poles of the systems and to improve the stability and speed of response compared with the conventional controls. This paper includes a detailed discussion of the effect of the gains of the controller on the root locus. The proposal is validated with simulation and experimental results.**

***Index Terms*—Complex control, *LCL* filter, root locus rules, three-phase inverter.**

I. Introduction

ELECTRIC-power applications (especially the renewable ones, such as photovoltaic, wind power, etc.) require high performance for injecting current into the power grid [1]. The use of power converters with an *LCL* filter has increased in recent years for grid-connection operations due to the better attenuation of the current harmonics and switching frequency in comparison with the traditional *L* filters [2]. On the other hand, power converters with *LCL* filters require more advanced control strategies, because the system order increases and a resonance peak appears that may cause stability problems in the presence of parameter variations [1].

Several control techniques have been applied to three-phase power converters with an *LCL* filter. The proposed methods include classical linear techniques, such as proportional-integral (PI) controllers [3], phase compensators [4], resonant controllers [5], linear Lyapunov tools [6], a state-feedback approach [7], linear quadratic regulators [8], and an linear–quadratic–Gaussian state-feedback controller with resonators [9]. Other examples include the model predictive control [10], the use of observers [11], and the pseudoderivative-feedback control method [12]. One of the most common approaches is the weighted average current control (WACC) strategy [13]. The WACC methodology has been recently studied by Dòria-Cerezo and Bodson [14] and also by Han *et al.* [15]. Also, nonlinear techniques have been used for *LCL* inverters. Examples include sliding mode control [16], [17], nonlinear feedback, and Poincaré analysis [18].

On the other hand, some papers propose controller designs for *LCL* inverters connected to unbalanced grids. Generally, the schemes involve controlling in parallel the positive and negative sequences. For example, He *et al.* [19] present a modified cascaded boundary-deadbeat control law for a four-wire inverter, Guo *et al.* [20] study the current injection without the need of phase-locked loop (PLL) calculation, or the work presented in [21] that also considers the operation under grid faults and the fault ride through capability. Other alternatives can be found in [22] that mix robust predictive control and sliding modes, in [23] and [24] wherein resonant controllers are considered, and in [25] wherein a pole placement technique is used.

In most cases, tuning the controller gains proceeds by trial and error, without a comprehensive understanding of the resulting dynamics. The main reason for this shortcoming is that *LCL* inverters are described by a sixth-order model in the *dq* or $\alpha\beta$ coordinates, so that the analysis of the closed-loop system is complicated. The objective of this paper is to improve the design methods and their analysis based on a complex description of the inverter.

The analysis of systems described by transfer functions with complex coefficients was first proposed by Novotny and Wouterse [26] and later used by Dalton and Gosbell [27] for the control and analysis of induction machines. Then, the approach was applied to current regulators in [28] and [29]. Some time later, an overview of applications to three-phase systems with complex transfer functions was published in [30]. Recently, Bodson [31] initiated a new effort by applying stability analysis tools and design techniques in the complex domain, which was extended in [32] and [33]. The main advantage is the reduction of the order of the system that facilitates the analysis and the synthesis of the controllers [34]. Recently, some frequency-domain results were revisited in [35]. Additionally, filters based on complex coefficients have been proposed for PLLs and synchronization techniques [36].

Manuscript received March 9, 2018; revised May 24, 2018; accepted July 2, 2018. Date of publication July 8, 2018; date of current version February 20, 2019. The work of A. Dòria-Cerezo was supported in part by the Government of Spain through the *Agencia Estatal de Investigación* Project DPI2017-85404-P and in part by the *Generalitat de Catalunya* through the Project 2017 SGR 872. Recommended for publication by Associate Editor A. Davoudi. *(Corresponding author: Arnau Dòria-Cerezo.)*

A. Dòria-Cerezo is with the Department of Electrical Engineering, Institute of Industrial and Control Engineering, Universitat Politècnica de Catalunya, 08028, Barcelona, Spain (e-mail: arnau.doria@upc.edu).

F. M. Serra is with the Laboratorio de Control Automático, Universidad Nacional de San Luis and CONICET, 5730, Villa Mercedes, San Luis, Argentina (e-mail: fserra@ieee.org).

M. Bodson is with the Department of Electrical and Computer Engineering, University of Utah, Salt Lake City, UT 84112-9206 USA (e-mail: marc.bodson@utah.edu).

Color versions of one or more of the figures in this paper are available online at http://ieeexplore.ieee.org.

Digital Object Identifier 10.1109/TPEL.2018.2854576

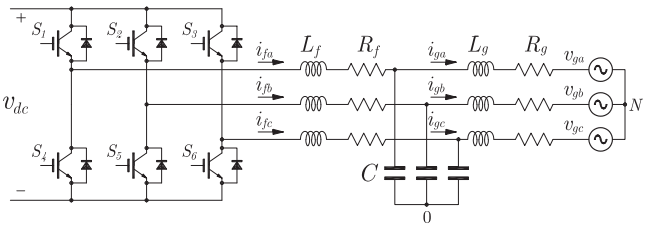

Fig. 1. Electrical scheme of a three-phase grid inverter connected with an *LCL* filter.

The root locus method was extended to the complex domain in [37], and its application to three-phase electrical systems was proposed in [14]. As a result of the simplification, it is possible to develop control schemes for which tuning rules can be provided for the control gains. The main contribution of this paper is the use of new control design tools for a power inverter using a complex transfer function description and the evaluation of the resulting feedback system on a real platform. With the use of complex-based techniques, the design and the analysis are simplified, converting the multiple-input multiple-output (MIMO) problem into a single-input single-output (SISO) problem. Compared with [14], the novelty of this paper comprises the following.

1) A detailed gain design/tuning method.
2) A study of the effect of parameter variations.
3) A control scheme considering the case of unbalanced grids.
4) A quantitative analysis of the effect of delays on the stability.
5) The implementation on a real platform, yielding experimental results.

This paper is organized as follows. Section II details the modeling procedure to obtain the transfer function with complex coefficients. The control design and the gain tuning discussion are presented in Section III. Then, some practical issues are considered in Section IV, including parametric variations, unbalanced grids, and the effect of feedback delays. Simulation and experimental results are presented in Section V and, finally, conclusions are stated in Section VI.

II. Three-Phase *LCL* Inverter Dynamical Model

A. Dynamical Model

A three-phase grid-connected inverter with an *LCL* filter is shown in Fig. 1. The dynamics of this system are described by

$$L_f \frac{\mathrm{d}\boldsymbol{i}_f^{\mathrm{abc}}}{\mathrm{d}t} = -R_f \boldsymbol{i}_f^{\mathrm{abc}} - \boldsymbol{M}\boldsymbol{v}_C^{\mathrm{abc}} + \frac{1}{2} v_{dc} \boldsymbol{M}\boldsymbol{u}^{\mathrm{abc}} \tag{1}$$

$$L_g \frac{\mathrm{d}\boldsymbol{i}_g^{\mathrm{abc}}}{\mathrm{d}t} = -R_g \boldsymbol{i}_g^{\mathrm{abc}} + \boldsymbol{M}\boldsymbol{v}_C^{\mathrm{abc}} - \boldsymbol{N}\boldsymbol{v}_g^{l} \tag{2}$$

$$C \frac{\mathrm{d}\boldsymbol{v}_C^{\mathrm{abc}}}{\mathrm{d}t} = \boldsymbol{i}_f^{\mathrm{abc}} - \boldsymbol{i}_g^{\mathrm{abc}} \tag{3}$$

where $\boldsymbol{i}_f^{\mathrm{abc}} = (i_{fa}, i_{fb}, i_{fc})^T$ and $\boldsymbol{i}_g^{\mathrm{abc}} = (i_{ga}, i_{gb}, i_{gc})^T$ are the inverter-side and the grid-side currents of the *LCL* filters, respectively, $\boldsymbol{v}_C^{\mathrm{abc}} = (v_{Ca}, v_{Cb}, v_{Cc})^T$ are the voltages in the filter capacitors, with capacitance C, and $\boldsymbol{v}_g^{l} = (v_g^{ab}, v_g^{bc})^T$ are the measured line-to-line voltages. The resistances R_f and R_g represent the losses in the filter inductors L_f and L_g. The control signals $\boldsymbol{u}^{\mathrm{abc}} = (u_a, u_b, u_c)^T$ take the discrete values $u_k \in \{-1, 1\}$, for $k = a, b, c$. The matrices $\boldsymbol{M}$ and $\boldsymbol{N}$ are given by

$$\boldsymbol{M} = \frac{1}{3}\begin{pmatrix} 2 & -1 & -1 \\ -1 & 2 & -1 \\ -1 & -1 & 2 \end{pmatrix}, \quad \boldsymbol{N} = \frac{1}{3}\begin{pmatrix} 2 & 1 \\ -1 & 1 \\ -1 & -2 \end{pmatrix}.$$

B. Complex Representation of the LCL Inverter

It is well known that a set of three-phase sinusoidal functions (electrical variables) $\boldsymbol{f}_{\mathrm{abc}} = (f_a(t), f_b(t), f_c(t))$, with the same frequency ω_g can be expressed as a sum of three sets of symmetrical variables as follows:

$$\boldsymbol{f}_{\mathrm{abc}} = \boldsymbol{f}_{\mathrm{abc}}^{0} + \boldsymbol{f}_{\mathrm{abc}}^{+} + \boldsymbol{f}_{\mathrm{abc}}^{-} \tag{4}$$

where in this case, because of the absence of a neutral connection, the zero-sequence is $\boldsymbol{f}_{\mathrm{abc}}^{0} = 0$. Similar to [14], the complex representation of (4) is obtained by applying the abc to $\alpha\beta$ transformation as follows:

$$f_{\alpha\beta} = f_\alpha + j f_\beta = \boldsymbol{T}\boldsymbol{f}_{\mathrm{abc}} \tag{5}$$

with[1] $\boldsymbol{T} = \sqrt{\frac{2}{3}}(1, e^{j\frac{2\pi}{3}}, e^{-j\frac{2\pi}{3}})$, and defining, we have

$$f_{dq}^{+} = f_d + j f_q = e^{-j\theta} f_{\alpha\beta} \tag{6}$$

$$f_{dq}^{-} = f_d + j f_q = e^{j\theta} f_{\alpha\beta} \tag{7}$$

where $\mathrm{d}\theta/\mathrm{d}t = \hat{\omega}_g$ and $\hat{\omega}_g$ is the estimated grid frequency.

Consequently, the dynamics (1)–(3) can be decomposed into two subsystems, for the positive (or forward) sequence as follows:

$$L_f \frac{\mathrm{d}i_f^{+}}{\mathrm{d}t} = -\big(R_f + j\omega_g L_f\big) i_f^{+} - v_c^{+} + v_{dc} u^{+} \tag{8}$$

$$L_g \frac{\mathrm{d}i_g^{+}}{\mathrm{d}t} = -\big(R_g + j\omega_g L_g\big) i_g^{+} + v_c^{+} - v_g^{+} \tag{9}$$

$$C \frac{\mathrm{d}v_c^{+}}{\mathrm{d}t} = i_f^{+} - i_g^{+} - j\omega_g C v_c^{+} \tag{10}$$

and for the negative (or backwards) sequence as follows:

$$L_f \frac{\mathrm{d}i_f^{-}}{\mathrm{d}t} = -\big(R_f - j\omega_g L_f\big) i_f^{-} - v_c^{-} + v_{dc} u^{-} \tag{11}$$

$$L_g \frac{\mathrm{d}i_g^{-}}{\mathrm{d}t} = -\big(R_g - j\omega_g L_g\big) i_g^{-} + v_c^{-} - v_g^{-} \tag{12}$$

$$C \frac{\mathrm{d}v_c^{-}}{\mathrm{d}t} = i_f^{-} - i_g^{-} + j\omega_g C v_c^{-} \tag{13}$$

where the state variables (omitting subindices $+$ and $-$) are $i_f = i_{fd} + j i_{fq}$, $i_g = i_{gd} + j i_{gq}$, and $v_c = v_{cd} + j v_{cq}$, the grid voltages are $v_g = v_{gd} + j v_{gq}$, and the control inputs are $u = u_d + j u_q$. As the dynamics (8)–(10) and (11)–(13) are similar, hereafter, the transfer function model and the control design

[1] Notice that we choose in (5) a power-preserving transformation.

are only detailed for the positive sequence.[2] The control design consists of separating the problem into two regulation schemes.

The open-loop dynamics (8)–(10) can be written as follows:

$$\begin{pmatrix} N_f(s) & 0 & 1 \\ 0 & N_g(s) & -1 \\ -1 & 1 & N_c(s) \end{pmatrix} \begin{pmatrix} i_f \\ i_g \\ v_c \end{pmatrix} = \begin{pmatrix} v_{dc}u \\ v_g \\ 0 \end{pmatrix}$$

where

$$N_f(s) = (s + j\omega_g)L_f + R_f \tag{14}$$

$$N_g(s) = (s + j\omega_g)L_g + R_g \tag{15}$$

$$N_c(s) = (s + j\omega_g)C. \tag{16}$$

Finally, the system has a complex transfer function, i.e.,

$$i_g = \frac{v_{dc}}{D_{OL}(s)}u + \frac{1 + N_f(s)N_c(s)}{D_{OL}(s)}v_g \tag{17}$$

where

$$D_{OL}(s) = N_f(s) + N_g(s) + N_f(s)N_g(s)N_c(s)$$

or, by splitting into the real and imaginary parts, we have

$$D_{OL}(s) = N_r(s) + jN_i(s) \tag{18}$$

with

$$\begin{aligned} N_r(s) &= CL_fL_gs^3 + C(L_fR_g + L_gR_f)s^2 \\ &\quad + (CR_fR_g - 3CL_fL_g\omega_g^2 + L_f + L_g)s \\ &\quad - \omega_g^2C(L_fR_g + L_gR_f) + R_f + R_g \end{aligned} \tag{19}$$

$$\begin{aligned} N_i(s) &= 3\omega_gCL_fL_gs^2 + 2C(L_fR_g\omega_g + L_gR_f\omega_g)s \\ &\quad - \omega_g^3CL_fL_g + \omega_gCR_fR_g + \omega_g(L_f + L_g). \end{aligned} \tag{20}$$

III. Control Design

In this section, the controller proposed in [14] is reviewed and a detailed discussion on the gain tuning procedure for a real application is proposed.

From (17), and treating v_g as a disturbance ($v_g = 0$), the complex transfer function of the system from the input u to the output i_g is given by

$$i_g = \frac{v_{dc}}{D_{OL}(s)}u. \tag{21}$$

A classical approach for controlling the *LCL* three-phase inverter is to decouple the d and q components [13]. This approach is helpful in tuning the PI gain parameters and implies the same closed-loop behavior for both dq components. The decoupling is obtained with a feedforward term cancelling all the cross-terms that, in the complex representation, are found in the imaginary part of $D_{OL}(s)$, i.e., $N_i(s)$. Based on this observation, the controller proposed in [14] consists of a conventional PI current controller plus a feedback on i_f, i.e.,

$$u = j\frac{N_i(s)}{v_{dc}}i_g - k_fi_f + k_P\left(1 + \frac{1}{T_is}\right)(i_g^{\text{ref}} - i_g) \tag{22}$$

[2]For simplicity, in the derived transfer function and control design, the subindices + are omitted.

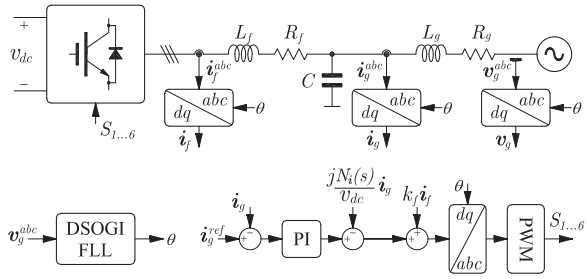

Fig. 2. Block diagram of the proposed controller.

where k_P and T_i are the control design (real) parameters and i_g^{ref} is the grid-side dq-current reference. In (22), k_f is a complex number that adds an extra degree of freedom to place the poles.

Inserting (22) in (21), we get

$$i_g = \frac{k_Pv_{dc}\left(s + \frac{1}{T_i}\right)}{D_{CL}(s)}i_g^{\text{ref}}$$

with

$$\begin{aligned} D_{CL}(s) &= sN_r(s) + sv_{dc}k_f(N_g(s)N_c(s) + 1) \\ &\quad + k_Pv_{dc}\left(s + \frac{1}{T_i}\right). \end{aligned}$$

Remark 1: The conventional PI current controller is recovered with $k_f = 0$, i.e.,

$$u = j\frac{N_i(s)}{v_{dc}}i_g + k_P\left(1 + \frac{1}{T_is}\right)(i_g^{\text{ref}} - i_g). \tag{23}$$

Fig. 2 shows the block diagram of the proposed controller. It mainly consists of a PI controller plus two additional feedback terms on i_g and i_f, which is similar to a classical state feedback scheme (see examples in [38], [24], and [9]). The current variables (in a complex description) i_g and i_f are obtained through the abc/dq transformations corresponding to (5) and (6) and (7).

Remark 2: The term $j[N_i(s)/v_{dc}]$ in (22) is noncausal. For implementation purposes, $N_i(s)$ can be approximated by the causal operator as follows:

$$N_i(s) \approx \frac{a_2s^2 + a_1s + a_0}{\epsilon_2s^2 + \epsilon_1s + 1}$$

where ϵ_2 and ϵ_1 are small values (see [39] for its digital implementation). For the experimental plant used in Section V, as the numerical coefficients of (20) are $a_2 = 3.239 \cdot 10^{-9}$, $a_1 = 1.036 \cdot 10^{-6}$, and $a_0 = 0.589$, $N_i(s)$ has been approximated by a static gain $N_i(s) \approx a_0$.

A. Root Locus Analysis

First, the influence of the control parameters on the root locus is analyzed. In particular, the case of the *LCL* inverter described in Section V is studied.

Fig. 3 shows the root locus when $k_f = 0$ for varying k_P and for different values of T_i. The open-loop poles are at the origin (pole p_1) and on the negative real axis (pole p_2), with two more complex poles having a negative real part (poles p_3 and p_4).

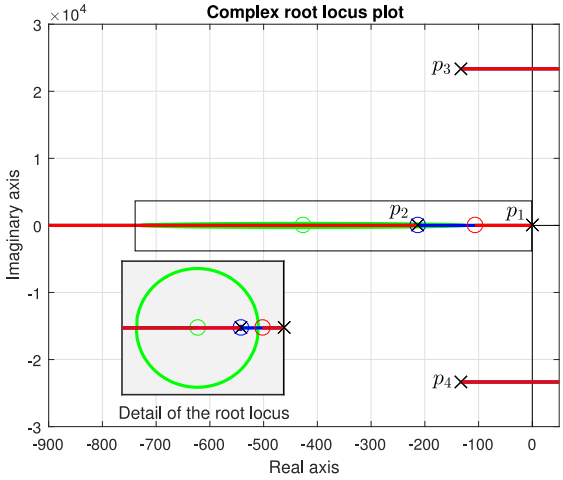

Fig. 3. Complex root locus plot of (23) with $k_f = 0$ for different values of T_i. $T_i = 0.5T_i^{\text{bk}}$ in green, $T_i = T_i^{\text{bk}}$ in blue, and $T_i = 2T_i^{\text{bk}}$ in red, where $T_i^{\text{bk}} = 0.00468$.

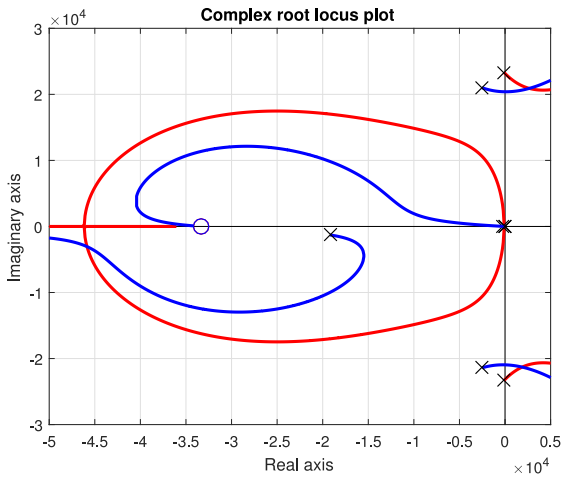

Fig. 4. Complex root locus: Comparison of the proposed controller (22) with $T_i = 3 \cdot 10^{-5}$ for $k_f = 0$ in red (conventional controller) and $k_f = 0.0989 + j0.007$ in blue.

Note that the poles p_3 and p_4 are close to the imaginary axis and, to maintain the stability of the system, the gain k_P must be sufficiently small. Moreover, following Rule 4 of the complex root locus method [37], a breakaway point exists for $T_i \leq 0.00468 = T_i^{\text{bk}}$, which can be viewed in the detail of the complex root locus shown in Fig. 3. Overall, the convergence speed is determined by the pole p_1 on the imaginary axis starting at the origin, but when raising k_P to increase the convergence speed, the complex poles p_3 and p_4 become unstable. This implies that only slow time responses can be achieved using the conventional PI structure (23).

Fig. 4 illustrates the comparison of the root locus for $k_f = 0$ and $k_f \neq 0$. The pole at the origin p_1 remains there, the pole p_2 moves out from the real axis and to the left, and poles p_3 and p_4 move to the left. For varying gain, p_1 goes to zero at $-1/T_i$, while p_2 goes to infinity asymptotically on the negative real axis. The two complex poles p_3 and p_4 still cross to the right-half plane before reaching asymptotes at $\pm 60^\circ$ (not shown). The main advantage is that the feedback on i_f moves the open-loop

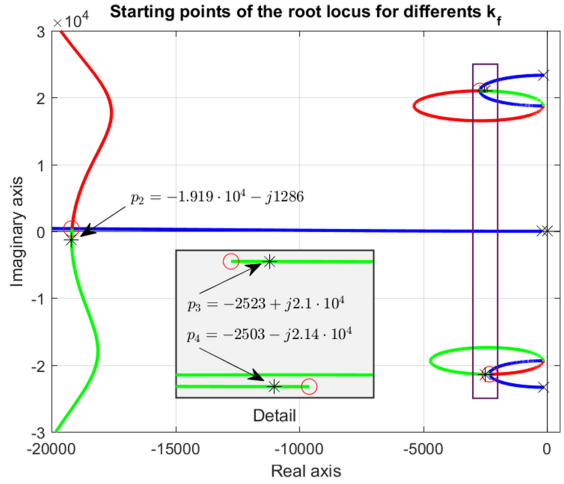

Fig. 5. Starting points ($k_P = 0$) of the root locus for the proposed controller in (22). ($\times$) poles are for $k_f = 0$, starting points for real k_f values are in blue, ($\circ$) poles are the farthest points from the real axis for a real k_f ($k_f = 0.0989$), the red and green plots are the roots for $k_f = 0.0989 + jk_{fI}$, $k_{fI} < 0$ and $k_{fI} > 0$, respectively, and ($*$) poles are for $k_f = 0.0989 + j0.007$.

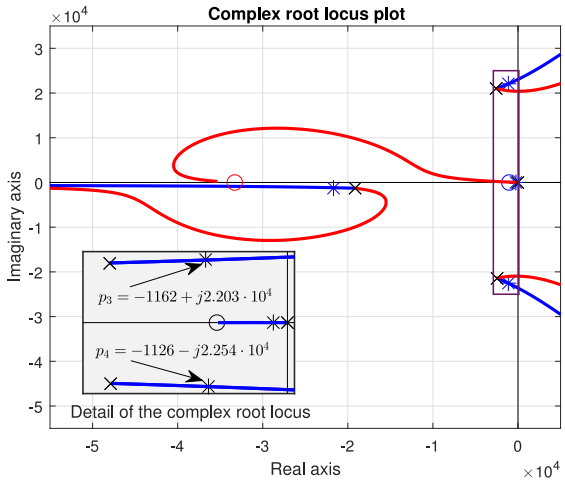

Fig. 6. Complex root locus of the complex-based controller for $k_f = 0.0989 + j0.007$ and different values of T_i. $T_i = 1 \cdot 10^{-3}$ (in blue) and $T_i = 3 \cdot 10^{-5}$ (in red). The selection of the poles for the specification is shown with star ($*$) marks.

poles p_3 and p_4 to a location farther in the left-half plane than for the conventional control law ($k_f = 0$).

Although the complex gain introduces an additional coupling between the d- and q-axes, it can be used to achieve better performances designing by the pole p_1 and by dominating all the other poles. In Fig. 5, the starting points (open-loop poles) of the root locus are shown for different values of k_f. The variation in the location of the starting points when k_f is a real number is shown in blue. The pole p_1 remains, but the other starting points move to the left, reaching a minimal value for p_3 and p_4 ($\circ$ marks). The imaginary part of k_f can also be tuned (red and green lines for negative and positive imaginary values, respectively), which affects the starting pole placement.

Finally, the effect of T_i is analyzed, as shown in Fig. 6. In all cases, the root locus is similar. The main difference is where the

zero $-1/T_i$ is placed and how the pole p_1 moves to $-1/T_i$. The choice of T_i can be related to the desired performance.

B. Control Gain Tuning

Gain tuning consists of finding the control parameters that provide the desired performance. For the application described in Section V, the desired settling time has been set at $t_s = 20$ ms (one power grid period) with minimal overshoot. As suggested by the analysis in the previous section, the pole p_1 can be used for the design (dominant pole) while placing the other poles further to the left.

The proposed procedure consists of the following four steps.

1) *Selection of the k_f gain:* As depicted in Fig. 5, k_f is selected such that the starting points of the poles other than p_1 are further from the imaginary axis. The minimal placement of the complex starting poles is reached with $k_f = 0.0989$ ($\circ$ marks) and, using the imaginary part, with $k_f = 0.0989 + j0.007$ ($*$ marks).
2) *Selection of the T_i gain:* Selecting a low T_i implies that the zero of the controller moves away from the imaginary axis, and the pole p_1 will move faster when k_P is increasing. Additionally, from Fig. 6, high T_i values imply that the branch for p_1, starting at the origin, remains close to the real axis. A tradeoff setting corresponds to $T_i = 1 \cdot 10^{-3}$ (blue line shown in Fig. 6), which gives a minimum overshoot and allows the selection of an appropriate k_P for the specifications.
3) *Selection of the k_P gain:* The gain k_P is selected such that the real part of the dominant pole p_1 is $\sigma = -200$. The value corresponds to $k_P = 0.025$.
4) *Verification:* Once the gains are obtained, the last step is to verify that the desired pole is dominant and, if necessary, to reduce the speed of the response. In this case, the closed-loop poles are placed at $p_1 = -201.1 + j11.46$ (dominant pole), $p_2 = -2.173 \cdot 10^4 - j1174$, $p_3 = -1162 + j2.203 \cdot 10^4$, and $p_4 = -1126 + j2.254 \cdot 10^4$, with star ($*$) marks as shown in Fig. 6. With a factor greater than 5 between the real part of the first pole and the real part of the other poles, no further change is found necessary.

IV. Analysis and Design Tools for Practical Issues

A. Robustness to Inductance Variations

This section analyzes the root locus in the presence of parametric variations of L_f and L_g. These variations originate from different causes, such as saturations, temperature effects, aging of the inductors, and others. Also, the influence of the grid impedance could be roughly accounted for as a variation of L_g (increasing).

Fig. 7 shows how the closed-loop poles move when L_f (red) and L_g (blue) change from 0.5 to 5 times the nominal values (these huge variations are considered in order to observe the effects). The poles obtained with the gains selected in the previous section are indicated with star marks ($*$), the closed-loop poles for 0.5 times the nominal value are marked with upside-down triangles ($\triangledown$), and the ones for 5 times the nominal value are denoted by square marks ($\square$).

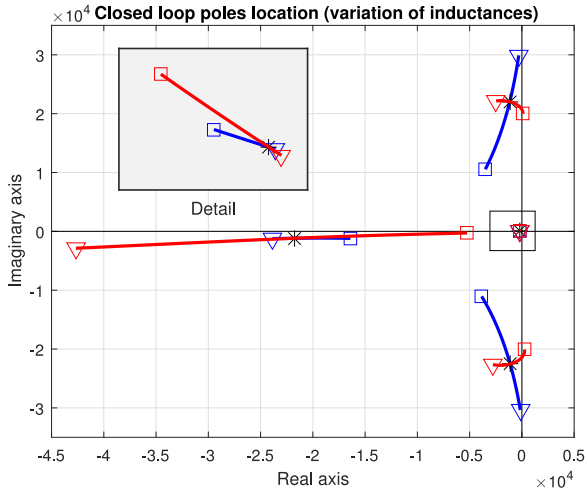

Fig. 7. Closed-loop poles' location of the complex-based controller for a variation in L_g and L_f between 0.5 and 5 times the nominal value. The poles for selected gains are indicated with star marks ($*$), the closed-loop poles for x0.5 the nominal value are marked with upside-down triangles ($\triangledown$), and the ones for x5 the nominal value are denoted by square marks ($\square$).

It can be seen that, when L_g increases, the dominant pole (p_1) moves to the left but remains close to the desired value. Poles p_3 and p_4 move to the left (increasing the stability), and p_2 moves to the right, but without affecting the dominance. When L_g is decreased, p_3 and p_4 move to the right. Also, p_1 slightly moves to the left, increasing the speed response (see the detail of the pole movement shown in Fig. 7). A similar discussion applies to variations of L_f. Notice that, even though poles p_2, p_3, and p_4 significantly move with variations of L_g and L_f, p_1 remains close to the nominal placement.

For the system considered in this paper, a typical variation (reduction of 10%) in L_g was tested and the following values were obtained: $p_1 = -201 + j11.45$, $p_2 = -2.207 \cdot 10^4 - j1182$, $p_3 = -1021 + j2.307 \cdot 10^4$, and $p_4 = -963.4 + j2.358 \cdot 10^4$. The dominance of p_1 with respect to p_2, p_3, and p_4 approximately remains. Thus, the desired performance of the designed controller is not significantly affected. In a case where the L_g variation compromises the performance, the abovementioned tuning procedure should be repeated with less restrictive requirements.

B. Design for Unbalanced Power Networks

The control scheme presented in Section III can be adapted to guarantee balanced grid currents by adding a loop for the negative current sequence [40]. The design follows the model derived in Section II, but using (11)–(13). The only difference is that (14)–(16) now yield

$$N_f(s) = (s - j\omega_g)L_f + R_f$$
$$N_g(s) = (s - j\omega_g)L_g + R_g$$
$$N_c(s) = (s - j\omega_g)C$$

and, consequently, (18) can now be expressed as

$$D_{OL}(s) = N_r(s) - jN_i(s)$$

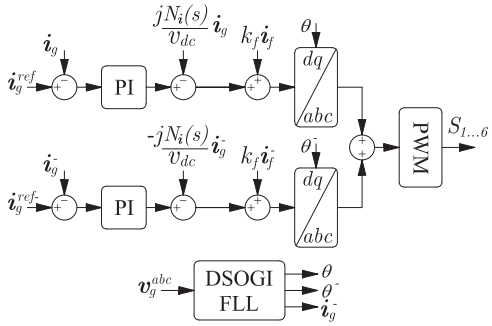

Fig. 8. Block diagram of the complete controller with the positive and negative sequence loops.

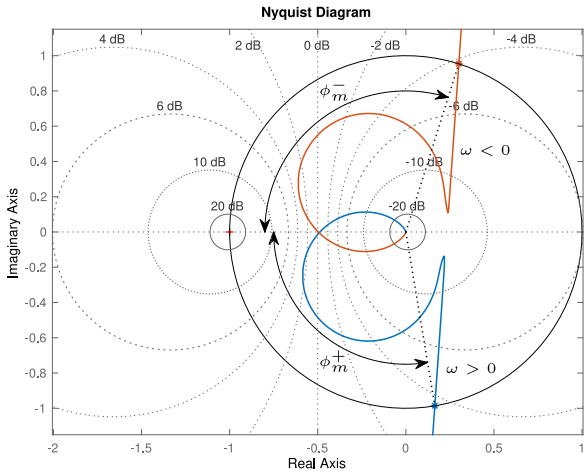

Fig. 9. Nyquist plot of $GH(j\omega)$ for $\omega > 0$ (in blue) and $\omega < 0$ (in red) using the parameters from Section V. The phase margins for the positive and negative frequencies are $\phi_m^+ = 1.736$ rad and $\phi_m^- = 1.876$ rad, respectively, with their corresponding crossover frequencies at $\omega_c^+ = 256.8$ rad/s and $\omega_c^- = -257.2$ rad/s.

where $N_r(s)$ and $N_i(s)$ are the same as (19) and (20). Notice that, for the negative sequence, the root locus is the conjugate of the one obtained for the positive sequence, and all the tuning procedures are similar.

Then, the proposed controller for the negative sequence is similar to (22), with a minus in the feedforward term, i.e.,

$$u^- = -j\frac{N_i(s)}{v_{dc}} i_g^- - k_f^- i_f^- + k_P^- \left(1 + \frac{1}{T_i^- s}\right)(i_g^{\text{ref}-} - i_g^-). \tag{24}$$

Overall, the control scheme is the addition of the two current loops (22) and (24), as shown in Fig. 8, where the dual second-order generalized integrator-frequency-locked loop (DSOGI-FLL) algorithm [41] is included to determine both positive and negative sequences. The DSOGI-FLL method together with the positive (or negative) sequence controller is a narrowband system centered around the positive (or negative) grid frequency. In particular, the components at plus (or minus) two times the grid frequency are approximately removed. This makes it possible to design the feedback loops for the two components separately, with the two control signals simply added together.

The gain tuning procedure of (24) is the same as the one described in Section III. In order to decouple the dynamics of the positive and negative sequences, it is recommended to design the negative sequence response as slower than the positive sequence. For the case considered in Section V, the desired settling time is set at $t_s = 200$ ms, and it can be obtained with $k_f^- = 0.0989 + j0.007, T_i^- = 10^{-3}$, and $k_P^- = 0.002$.

C. Robustness in the Presence of Time Delays

Delays appear in a feedback loop due to the filter on the currents and the sampled data system. The effect of these delays on the stability can be studied by including the dynamics of the filter and a Padé approximation of the delay in the procedure described in Section III. An interesting option provided by the complex analysis is to compute the delay margin of the feedback system based on the phase of the complex loop transfer function at the crossover frequency (or frequencies) [30]. The computation of the delay margin originates from the Nyquist criterion and can interpreted from the Nyquist plot as for transfer functions with real coefficients. However, some adjustments need to be made because the Nyquist plots of complex transfer functions for positive and negative frequencies are not necessarily the complex conjugates of each other.

To compute the delay margin, the complex loop transfer function $GH(s)$ is obtained from (21) using (22) as follows:

$$GH(s) = \frac{\boldsymbol{i}_g}{\boldsymbol{i}_g^{ref} - \boldsymbol{i}_g} = k_P \frac{v_{dc}\left(s + \frac{1}{T_i}\right)}{s\left(N_r(s) + v_{dc}k_f\left(1 + N_c(s)N_g(s)\right)\right)} \tag{25}$$

where (15) and (16) have been used. Fig. 9 shows the Nyquist plot[3] of $GH(j\omega)$ for $-\infty < \omega < \infty$.

The phase margin is determined from the intersection of the Nyquist plot with a circle of radius 1 centered at $(-1, 0)$, and it can be computed numerically. To address the differences between the real and complex transfer function cases, we define the phase margin as the angle $\phi_m \in (-\pi, \pi)$ such that

$$-e^{j\phi_m} = GH(j\omega_c) \tag{26}$$

where ω_c is the crossover frequency such that $|GH(j\omega_c)| = 1$. In this manner, ϕ_m can be positive or negative (for phase delay or phase advance), and an interval is obtained for the phase margin using the intersections for positive and negative frequencies (denoted by ϕ_m^+ and ϕ_m^-, respectively). Since a delay T_d corresponds to a phase delay of ωT_d, a phase margin ϕ_m corresponds to a delay margin given by

$$T_d = \frac{\phi_m}{\omega_c}. \tag{27}$$

Applying these concepts to the system with the parameters from Section V, we get that the phase margins are $\phi_m^+ = 1.736$ rad and $\phi_m^- = -1.876$ rad, with crossover frequencies $\omega_c^+ = 256.8$ rad/s and $\omega_c^- = -257.2$ rad/s. This

[3]The MATLAB `nyquist` command does not work for complex transfer functions because the function only computes the polar plot for positives frequencies (and then takes the symmetric curve for the negatives ones).

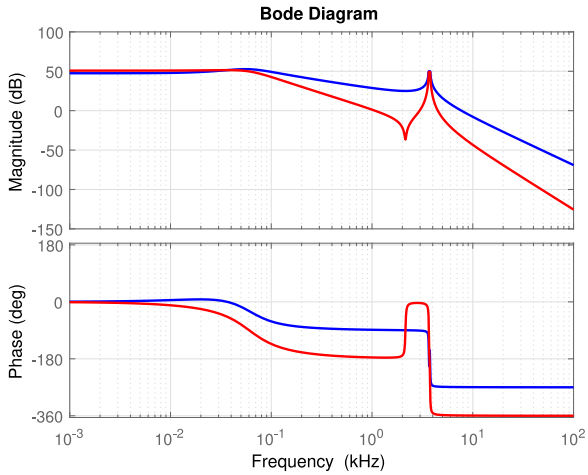

Fig. 10. Bode plots of $G_r(s)$ and $G_i(s)$.

corresponds to delay margins $T_d^+ = 6.7$ ms and $T_d^- = 7.3$ ms. Therefore, an overall delay margin of 6.7 ms is obtained. The delay is far greater than the delay associated with sampling (0.05 ms for 20 kHz; see Section V) or with the current filter (less than 1μs for a digital signal processor (DSP) running at 160 MHz). Additionally, the gain margins are satisfactory $g_m^+ = 5.96$ dB and $g_m^- = 5.81$ dB (see Fig. 9) and give an overall gain margin of 5.81 dB. The same analysis for the negative feedback control loop (24) gives even higher delay margins $T_d^+ = 76.3$ ms and $T_d^- = 83.3$ ms.

V. Simulation and Experimental Results

The proposed control strategy has been validated through simulation and experimental results. The simulation tests were performed using a complete model of the system, which includes losses in the power converter and switching effects. Moreover, the experimental results were obtained using an *LCL* inverter laboratory prototype. The parameters used in the simulation match those of the experimental system and are as follows: $v_{dc} = 300$ V, $v_{ll} = 175$ V, $L_f = 1.25$ mH, $L_g = 0.625$ mH, $R_f = 0.2\omega_g$, $R_g = 0.2\omega_g$, and $C = 4.4$ μF, with a resistor of $R_c = 100\,\text{k}\Omega$ in parallel to damp the resonance of the *LCL* filter.

For a practical implementation, where a switched action is required, a frequency analysis is necessary to avoid resonance phenomena due to the switching frequency. From (17), we can deduce that

$$i_g = \frac{v_{dc}(N_r(s) - jN_i(s))}{N_r^2(s) + N_i^2(s)}u = \big(G_r(s) + jG_i(s)\big)u$$

where

$$G_r(s) = \frac{v_{dc}N_r(s)}{N_r^2(s) + N_i^2(s)}, \quad G_i(s) = \frac{v_{dc}N_i(s)}{N_r^2(s) + N_i^2(s)}.$$

Fig. 10 shows the Bode plots of $G_r(s)$ (blue) and $G_i(s)$ (red). Notice that a first resonance peak appears close to 50 Hz and a pair of resonance peaks at around 3.5 kHz. This suggests a commutation at higher frequencies, and the switching frequency of the pulsewidth modulation strategy was set at 20 kHz.

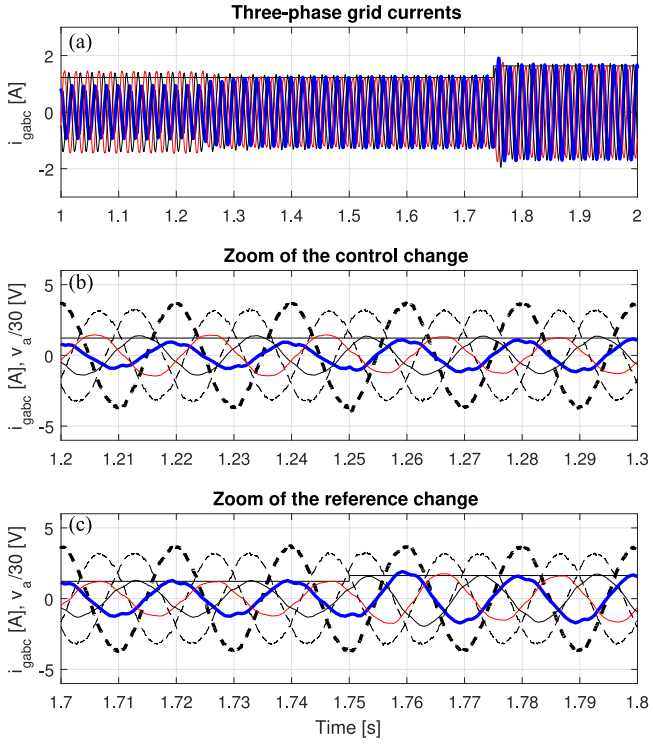

Fig. 11. Simulation results: Grid currents for a grid current reference change and negative sequence control. (a) Grid current in *abc* coordinates. (b) Voltage and current of the system when activating the control of negative sequence. (c) Voltage and current of the system for a change in the current reference.

A. Simulation Results

With the aim of considering a realistic scenario in the simulation tests, the grid voltage has 2% of a fifth harmonic, 1% of a seventh harmonic, and 10% of unbalance (calculated according to IEC standard). In addition, parameter variations in the *LCL* filter were considered (10% in L_f, L_g, R_f, and R_g). The simulated test comprises the following three different scenarios.

1) From $t = 1$ s, only the positive sequence is regulated with a current reference of 1.225 A and unity power factor, corresponding to[4] $i_{gd}^{\text{ref}} = 1.5$ A and $i_{gq}^{\text{ref}} = 0$ A.
2) From $t = 1.25$ s, the control of the negative sequence controller, i.e., the proposed negative sequence control (24) is turned-ON, with $i_{gd}^{\text{ref}-} = i_{gq}^{\text{ref}-} = 0$ A.
3) From $t = 1.75$ s, a step change $i_{gd}^{\text{ref}} = 2$ A and $i_{gq}^{\text{ref}} = 0$.

Figs. 11 and 12 show the three-phase currents and the positive and negative sequences of the grid currents during the test, respectively. Also, Fig. 11 includes a zoom-in view of the transient between scenarios from A to B and from B to C. It can be noticed how, initially, the proposed control scheme regulates only the positive sequence of the grid currents i_g at the desired values but, as expected, they are unbalanced. From $t = 1.25$ s, the grid currents become balanced with the designed settling

[4]The difference between the maximum value of i_{ga} and i_{gd} is because the power invariant abc/dq transformation was used in the implementation of the controller [see (5)].

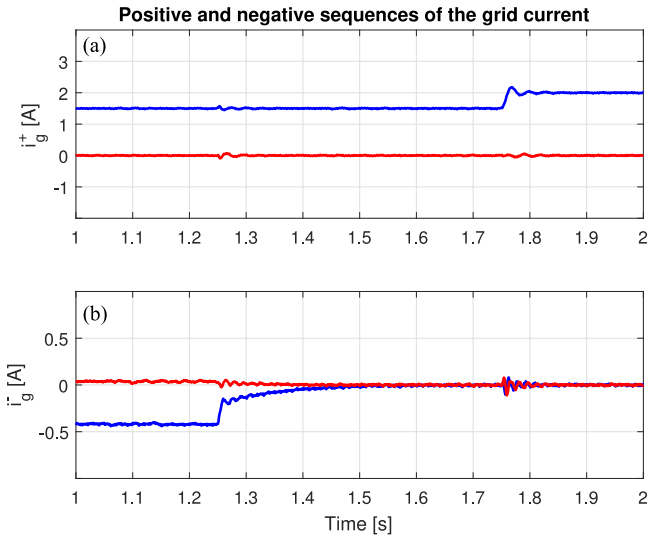

Fig. 12. Simulation results: Positive and negative sequences of the grid currents in dq coordinates. (a) i_{gd} and i_{gq}. (b) i_{gd}^{-} and i_{gq}^{-}.

time of 0.2 s. Then, at $t = 1.75$ s, the reference of the d-axis grid current i_{gd}^{ref} changes from 1.5 to 2 A, while $i_{gq}^{\text{ref}} = 0$. The control response, shown in Figs. 11 and 12, exhibits a time response with less than one grid period and a small overshoot, as expected.

B. Experimental Tests

The experimental tests were performed using an *LCL* three-phase grid inverter laboratory prototype with the estimated parameters used during the simulation stage. The inverter has a semix-101GD12E4s module of Semikron (1200 V, 100 A) and the controller algorithm was implemented in a TMS320F28335 floating point DSP of Texas Instrument. Fig. 13 shows the testbench, including the inverter and the microcontroller. All tests in this section were performed using a real grid voltage with 2.63% of total harmonic distortion (THD) and 6% of unbalance calculated according to IEC standard. The tests that were carried out are the same as the simulation tests presented in the previous section with scenarios A, B, and C.

Fig. 14(a) and (b) shows the grid currents for the positive and negative sequences, respectively, during the test. It can be observed that, between 1 and 1.25 s, the controller regulates the dq-currents i_{gd} and i_{gq} with the desired performance. Nevertheless, the grid currents are unbalanced because the control of the negative sequence is not used. From $t = 1.25$ s, when the control of the negative sequence is turned-ON, the grid currents become balanced in the specified time. In the same test, at $t = 1.75$ s, the reference of the d-axis grid current i_{gd}^{ref} changes from 1.5 to 2 A, while $i_{gq}^{\text{ref}} = 0$. The control response is as expected, with approximately one grid period and a small overshoot.

Figs. 15 and 16 plot the steady-state currents before and after the control of the negative sequence current is engaged. As expected, the currents are balanced, even though the grid voltages are unbalanced, when the negative sequence control is ON.

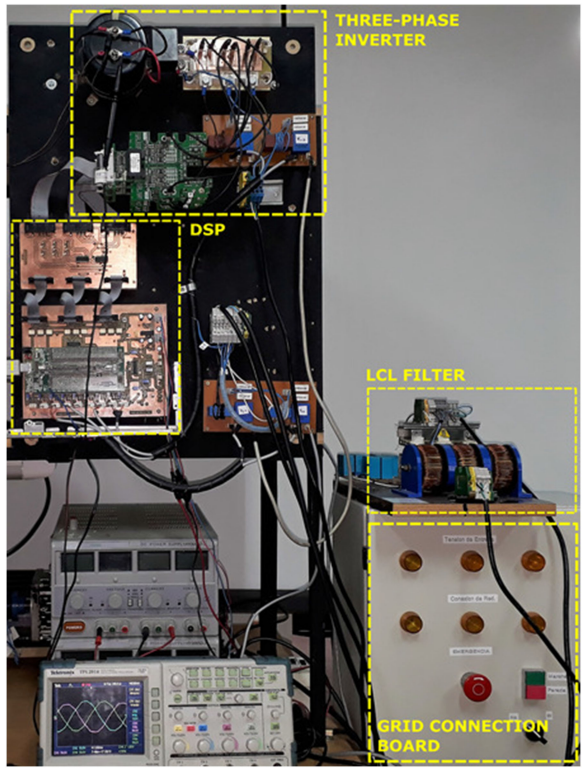

Fig. 13. Experimental testbench.

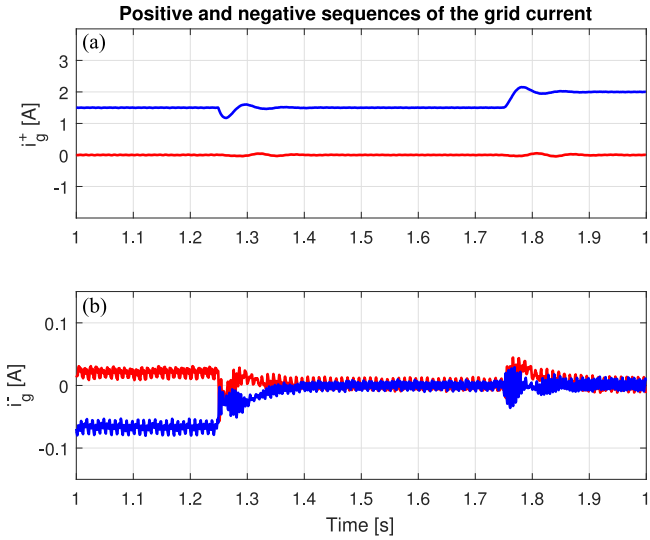

Fig. 14. Experimental results: Positive and negative sequences of the grid currents in dq coordinates. (a) i_{gd} and i_{gq}. (b) i_{gd}^{-} and i_{gq}^{-}.

The behavior of the three-phase grid currents for a change of the reference current (from $i_{gd}^{\text{ref}} = 1.5$ to 2 A) is illustrated in Fig. 17. As can be observed, the time response of the currents to the step change corresponds to the desired value, i.e., one grid period.

Finally, Fig. 18 shows a detail of the grid voltage and current for phase a when $i_{gd}^{\text{ref}} = 2$ A and $i_{gq}^{\text{ref}} = 0$ A (unity power factor). In the steady state, the grid current has a low distortion and is

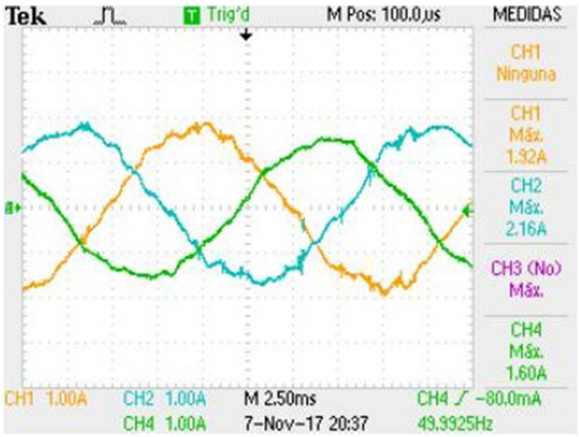

Fig. 15. Experimental results: Three-phase grid currents in the steady state when the control of the negative sequence is OFF.

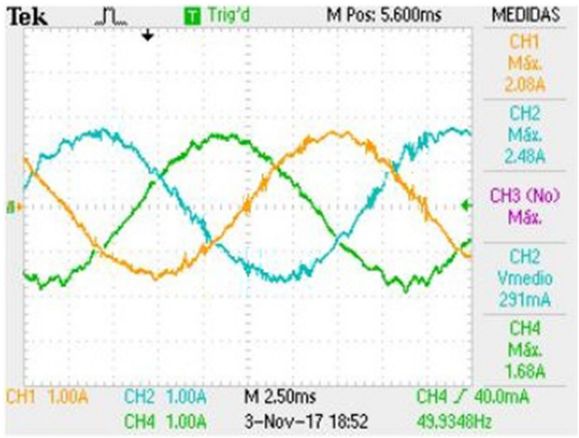

Fig. 16. Experimental results: Three-phase grid currents in the steady state when the control of the negative sequence is turned-ON.

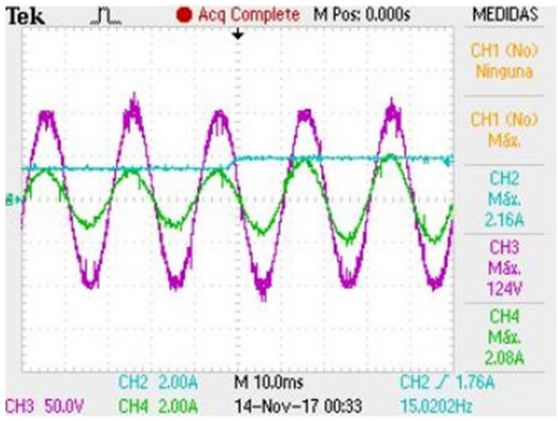

Fig. 17. Experimental results: Grid voltage (blue) and transient of the grid current (red) for a step change in i_{gd}^{ref} from 1.5 to 2 A (magenta).

in phase with the voltage. As shown in Fig. 19, even though the controller only considers the fundamental (with both positive and negative sequences), the THD of the current is 2.76% (within the standard values, i.e., below 5%), which is mainly due to the THD of the voltage grid.

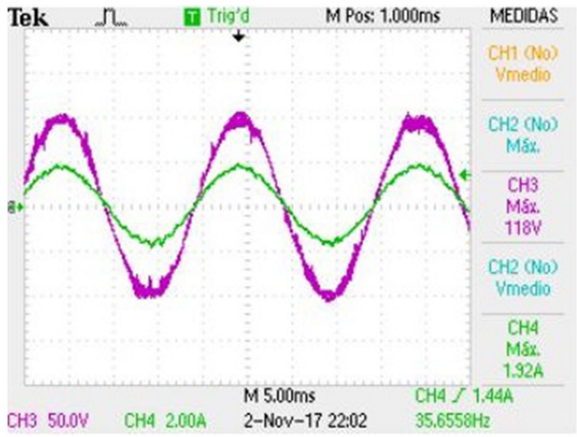

Fig. 18. Experimental results: Grid voltage (blue) and steady-state grid current (red) for $i_{gd}^{\text{ref}} = 2.5$ A.

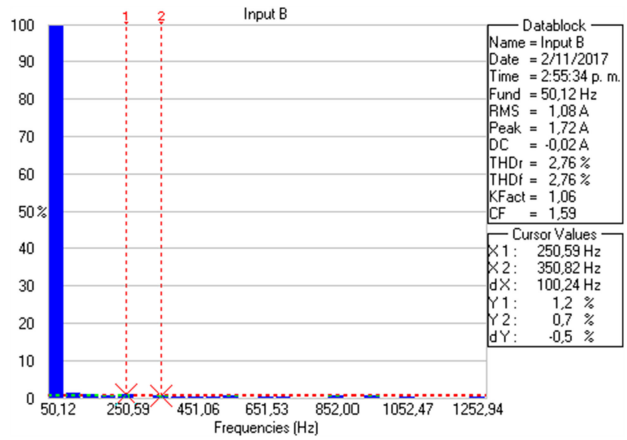

Fig. 19. Experimental results: Frequency spectrum corresponding to the grid current shown in Fig. 18.

VI. Conclusion

This paper uses a new approach for the design of controllers in electrical power systems based on the description of the dynamics using transfer functions with complex coefficients. The methodology has been applied to a three-phase grid inverter with an *LCL* filter, including practical scenarios such as parameter variations, unbalanced grids, and the effect of delays. The use of the complex description of the plant allows one to explore alternatives to the approaches reported in the literature. In particular, the use of SISO tools for a MIMO problem implies that the typical decoupling term is not necessary. In fact, the resulting design suggests a coupling of the dq-coordinates by means of a complex value of k_f, moving the starting poles of the root locus to the left and improving the stability margin. The design procedure was detailed, including discussions on the root locus. Both simulations and experimental results validate the controller design and show the usefulness of the proposed gain-tuning procedure for achieving the desired performance. Future works would include the use of the presented approach for systems with high THD, as well as its application to other electrical power systems.

REFERENCES

[1] R. Teodorescu, M. Liserre, and P. Rodríguez, *Grid Converters for Photovoltaic and Wind Power Systems*. Hoboken, NJ, USA: Wiley, 2011.

[2] M. Castilla, J. Miret, A. Camacho, J. Matas, and L. de Vicuña, "Reduction of current harmonic distortion in three-phase grid-connected photovoltaic inverters via resonant current control," *IEEE Trans. Ind. Electron.*, vol. 60, no. 4, pp. 1464–1473, Apr. 2013.

[3] X. Zhang, P. Chen, C. Yu, F. Li, H. Thanh-Do, and R. Cao, "Study of a current control strategy based on multisampling for high-power grid-connected inverters with an LCL filter," *IEEE Trans. Power Electron.*, vol. 32, no. 7, pp. 5023–5034, Jul. 2017.

[4] D. Pan, X. Ruan, C. Bao, W. Li, and X. Wang, "Optimized controller design for LCL-type grid-connected inverter to achieve high robustness against grid-impedance variation," *IEEE Trans. Ind. Electron.*, vol. 62, no. 3, pp. 1537–1547, Mar. 2015.

[5] R. Fantino, C. Busada, and J. Solsona, "Optimum PR control applied to LCL filters with low resonance frequency," *IEEE Trans. Power Electron.*, vol. 33, no. 1, pp. 793–801, Jan. 2018.

[6] H. Komurcugil, N. Altin, S. Ozdemir, and I. Sefa, "Lyapunov-function and proportional-resonant-based control strategy for single-phase grid-connected VSI with LCL filter," *IEEE Trans. Ind. Electron.*, vol. 63, no. 5, pp. 2838–2849, May 2016.

[7] C. Busada, S. Gomez-Jorge, and J. Solsona, "Full-state feedback equivalent controller for active damping in LCL-filtered grid-connected inverters using a reduced number of sensors," *IEEE Trans. Ind. Electron.*, vol. 62, no. 10, pp. 5993–6002, Oct. 2015.

[8] S. A. Khajehoddin, M. Karimi-Ghartemani, and M. Ebrahimi, "Optimal and systematic design of current controller for grid-connected inverters," *IEEE J. Emerg. Sel. Topics Power Electron.*, vol. 6, no. 2, pp. 812–824, Jun. 2018.

[9] F. Huerta, J. Pérez, S. Cóbreces, and M. Rizo, "Frequency-adaptive multi-resonant LQG state-feedback current controller for LCL- filtered VSCs under distorted grid voltages," *IEEE Trans. Ind. Electron.*, vol. 65, no. 11, pp. 8433–8444, Nov. 2018.

[10] X. Zhang, Y. Wang, C. Yu, L. Guo, and R. Cao, "Hysteresis model predictive control for high-power grid-connected inverters with output LCL filter," *IEEE Trans. Ind. Electron.*, vol. 63, no. 1, pp. 246–256, Jan. 2016.

[11] B. Wang, Y. Xu, Z. Shen, J. Zou, C. Li, and H. Liu, "Current control of grid-connected inverter with LCL filter based on extended-state observer estimations using single sensor and achieving improved robust observation dynamics," *IEEE Trans. Ind. Electron.*, vol. 64, no. 7, pp. 5428–5439, Jul. 2017.

[12] J. Wang, J. Yan, and L. Jiang, "Pseudo-derivative-feedback current control for three-phase grid-connected inverters with LCL filters," *IEEE Trans. Power Electron.*, vol. 31, no. 5, pp. 3898–3912, May 2016.

[13] N. He *et al.*, "Weighted average current control in a three-phase grid inverter with an LCL filter," *IEEE Trans. Power Electron.*, vol. 28, no. 6, pp. 2785–2797, Jun. 2013.

[14] A. Dòria-Cerezo and M. Bodson, "Design of controllers for electrical power systems using a complex root locus method," *IEEE Trans. Ind. Electron.*, vol. 63, no. 6, pp. 3706–3716, Jun. 2016.

[15] Y. Han, Z. Li, P. Yang, C. Wang, L. Xu, and J. Guerrero, "Analysis and design of improved weighted average current control strategy for LCL-type grid-connected inverters," *IEEE Trans. Energy Convers.*, vol. 32, no. 3, pp. 941–952, Sep. 2017.

[16] D. Biel, A. Dòria-Cerezo, V. Repecho, and E. Fossas, "Sliding mode control of a three-phase three-wire LCL rectifier," in *Proc. IEEE 23rd Int. Symp. Ind. Electron.*, 2014.

[17] R. Guzman, L. G. de Vicuña, M. Castilla, J. Miret, and J. de la Hoz, "Variable structure control for three-phase LCL-filtered inverters using a reduced converter model," *IEEE Trans. Ind. Electron.*, vol. 65, no. 1, pp. 5–15, Jan. 2018.

[18] S. Eren, M. Pahlevaninezhad, A. Bakhshai, and P. Jain, "Composite nonlinear feedback control and stability analysis of a grid-connected voltage source inverter with LCL filter," *IEEE Trans. Ind. Electron.*, vol. 60, no. 11, pp. 5059–5074, Nov. 2013.

[19] Y. He, H. S.-H. Chung, C. N.-M. Ho, and W. Wu, "Modified cascaded boundary-deadbeat control for a virtually-grounded three-phase grid-connected inverter with LCL filter," *IEEE Trans. Power Electron.*, vol. 32, no. 10, pp. 8163–8180, Oct. 2017.

[20] X. Guo, W. Liu, X. Zhang, X. Sun, Z. Lu, and J. M. Guerrero, "Flexible control strategy for grid-connected inverter under unbalanced grid faults without PLL," *IEEE Trans. Power Electron.*, vol. 30, no. 4, pp. 1773–1778, Apr. 2015.

[21] X. Guo, W. Liu, and Z. Lu, "Flexible power regulation and current-limited control of the grid-connected inverter under unbalanced grid voltage faults," *IEEE Trans. Ind. Electron.*, vol. 64, no. 9, pp. 7425–7432, Sep. 2017.

[22] Y. A.-R. I. Mohamed, "Mitigation of dynamic, unbalanced, and harmonic voltage disturbances using grid-connected inverters with LCL filter," *IEEE Trans. Ind. Electron.*, vol. 58, no. 9, pp. 3914–3924, Sep. 2011.

[23] Z. Xin, P. Mattavelli, W. Yao, Y. Yang, F. Blaabjerg, and P. Loh, "Mitigation of grid current distortion for LCL-filtered voltage source inverter with inverter current feedback control," *IEEE Trans. Power Electron.*, vol. 33, no. 7, pp. 6248–6261, Jul. 2018.

[24] N.-B. Lai and K.-H. Kim, "Robust control scheme for three-phase grid-connected inverters with LCL-filter under unbalanced and distorted grid conditions," *IEEE Trans. Energy Convers.*, vol. 33, no. 2, pp. 506–515, Jun. 2018.

[25] D. Pérez-Estévez, J. Doval-Gandoy, A. Yepes, and O. López, "Positive- and negative-sequence current controller with direct discrete-time pole placement for grid-tied converters with LCL filter," *IEEE Trans. Power Electron.*, vol. 32, no. 9, pp. 7207–7221, Sep. 2017.

[26] D. Novotny and J. H. Wouterse, "Induction machine transfer functions and dynamic response by means of complex time variables," *IEEE Trans. Power App. Syst.*, vol. 95, no. 4, pp. 1325–1335, Jul. 1976.

[27] P. Dalton and V. Gosbell, "A study of induction motor current control using the complex number representation," in *Proc. IEEE Ind. Appl. Soc. Annual Meeting*, 1989, pp. 355–361.

[28] S. Gataric and N. Garrigan, "Modeling and design of three-phase systems using complex transfer functions," in *Proc. 30th Annu. IEEE Power Electron. Spec. Conf.*, 1999, pp. 691–697.

[29] F. B. del Blanco, M. W. Degner, and R. D. Lorenz, "Dynamic analysis of current regulators for AC motors using complex vectors," *IEEE Trans. Ind. Appl.*, vol. 35, no. 6, pp. 1424–1423, Nov./Dec. 1999.

[30] L. Harnefors, "Modeling of three-phase dynamic systems using complex transfer functions and transfer matrices," *IEEE Trans. Ind. Electron.*, vol. 54, no. 4, pp. 2239–2248, Aug. 2007.

[31] M. Bodson, "The complex Hurwitz test for the stability analysis of induction generators," in *Proc. Amer. Control Conf.*, 2010, pp. 2539–2544.

[32] M. Bodson and O. Kiselychnyk, "The complex Hurwitz test for the analysis of spontaneous self-excitation in induction generators," *IEEE Trans. Autom. Control*, vol. 58, no. 2, pp. 449–454, Feb. 2013.

[33] A. Dòria-Cerezo, M. Bodson, C. Batlle, and R. Ortega, "Study of the stability of a direct stator current controller for a doubly-fed induction machine using the complex Hurwitz test," *IEEE Trans. Control Syst. Technol.*, vol. 21, no. 6, pp. 2323–2331, Nov. 2013.

[34] M. Bodson, "Design of controllers in the complex domain," in *Proc. 53rd IEEE Conf. Decis. Control*, 2014, pp. 4077–4082.

[35] O. Troeng, B. Bernhardsson, and C. Rivetta, "Complex-coefficient systems in control," in *Proc. Amer. Control Conf.*, 2017, pp. 1721–1727.

[36] X. Guo, W. Wu, and Z. Chen, "Multiple-complex coefficient-filter-based phase-locked loop and synchronization technique for three-phase grid-interfaced converters in distributed utility networks," *IEEE Trans. Ind. Electron.*, vol. 58, no. 4, pp. 1194–1204, Apr. 2011.

[37] A. Dòria-Cerezo and M. Bodson, "Root locus rules for polynomials with complex coefficients," in *Proc. 21st Mediterranean Conf. Control Automat.*, 2013, pp. 663–670.

[38] J. Dannehl, F. Fuchs, and P. Thogersen, "PI state space current control of grid-connected PWM converters with LCL filters," *IEEE Trans. Power Electron.*, vol. 25, no. 9, pp. 2320–2330, Sep. 2010.

[39] A. Dabroom and H. K. Khalil, "Numerical differentiation using high-gain observers," in *Proc. 36th IEEE Conf. Decis. Control*, 1997, pp. 4790–4795.

[40] A. Yazdani and R. Iravani, "A unified dynamic model and control for the voltage-sourced converter under unbalanced grid conditions," *IEEE Trans. Power Del.*, vol. 21, no. 3, pp. 1620–1629, Jul. 2006.

[41] P. Rodríguez, A. Luna, I. Candela, R. Mujal, R. Teodorescu, and F. Blaabjerg, "Multiresonant frequency-locked loop for grid synchronization of power converters under distorted grid conditions," *IEEE Trans. Ind. Electron.*, vol. 58, no. 1, pp. 127–138, Jan. 2011.

Arnau Dòria-Cerezo was born in Barcelona, Spain, in 1974. He received the undergraduate degree in electromechanical engineering and the Ph.D. degree in advanced automation and robotics from the Universitat Politècnica de Catalunya (UPC), Barcelona, in 2001 and 2006, respectively, and the D.E.A. degree in industrial automation from the Institut National des Sciences Appliquées de Lyon, Villeurbanne, France, in 2001.

He is currently an Associate Professor with the Department of Electrical Engineering, UPC, and also with the Advanced Control of Energy Systems Group, Institute of Industrial and Control Engineering, UPC. From 2003 to 2004, he was a Control Training Site-Research Fellow with the Laboratoire des Signaux et Systèmes, Supélec, France. In 2010, he was a visitor at the Technische Universiteit Delft, Delft, The Netherlands. His research interests include modeling and control of electrical systems and automotive applications.

Since 2017, Dr. Dòria-Cerezo has been an Associate Editor for *Control Engineering Practice*.

Federico Martín Serra (M'17) was born in Villa Mercedes, San Luis, Argentina, in 1981. He received the Electrical and Electronics Engineering degree from the Universidad Nacional de San Luis, San Luis, Argentina, in 2007 and the Doctor of Engineering degree from the Universidad Nacional de Río Cuarto, Río Cuarto, Argentina, in 2013.

Since 2012, he has been the Director of the Laboratory of Automatic Control, Universidad Nacional de San Luis. He is currently a Professor with the Universidad Nacional de San Luis and also an Assistant Researcher with Consejo Nacional de Investigaciones Científicas y Técnicas, Buenos Aires, Argentina. His research interests include modeling and advanced control of power converters in applications of microgrids, electric vehicles, and renewable energy conversion systems.

Marc Bodson (F'06) received the Ingénieur Civil Mécanicien et Electricien degree from the Université Libre de Bruxelles, Brussels, Belgium, in 1980, two M.S. degrees, one in electrical engineering and computer science and another in aeronautics and astronautics, from the Massachusetts Institute of Technology, Cambridge, MA, USA, in 1982, and the Ph.D. degree in electrical engineering and computer science from the University of California at Berkeley, Berkeley, CA, USA, in 1986.

He is currently a Professor in Electrical and Computer Engineering with the University of Utah, Salt Lake City, UT, USA. He was the Chair of the Department of Electrical and Computer Engineering, University of Utah, from 2003 to 2009. His research interests include adaptive control with applications to electromechanical systems and aerospace.

Dr. Bodson was elected Associate Fellow of the AIAA in 2013. He was a Belgian American Educational Foundation Fellow in 1980 and a Lady Davis Fellow with the Technion, Haifa, Israel, in 1990. He was the Editor-in-Chief for the IEEE TRANSACTIONS ON CONTROL SYSTEMS TECHNOLOGY from 2000 to 2003.